LASER & PHOTONICS REVIEWS

www.lpr-journal.org

Mode and Polarization-Division Multiplexing Based on Silicon Nitride Loaded Lithium Niobate on Insulator Platform

Xu Han, Yongheng Jiang, Andreas Frigg, Huifu Xiao, Pu Zhang, Thach Giang Nguyen, Andreas Boes, Jianhong Yang, Guanghui Ren, Yikai Su, Arnan Mitchell, and Yonghui Tian**

Mode and polarization-division multiplexing technologies (MDM and PDM) can offer considerable parallelism for optical multiplexing biosensors, complex optical neural networks, and high-capacity optical interconnects, while requiring only a single-wavelength laser source. Thanks to the mature fabrication processes of silicon nitride and superior material properties of lithium niobate, the silicon nitride loaded lithium niobate on insulator (LNOI) platform allows the integration of high-speed optical modulators and optical (de)multiplexing devices to achieve high-capacity and low-cost photonic integrated circuits suitable for data communication applications. In this contribution, MDM and PDM are investigated in a silicon nitride loaded LNOI (X-cut) platform. As a proof of concept, an asymmetrical directional coupler-based mode (de)multiplexer (MMUX) and polarization splitter-rotator (PSR) are designed, fabricated, and experimentally demonstrated. The measured insertion losses are lower than 1.46 and 1.49 dB, while the inter-modal crosstalk is lower than −13.03 and −17.75 dB for the MMUX and PSR, respectively, for a wavelength range of 1525–1565 nm. A 40 Gbps data transmission experiment demonstrates the data transmission capabilities of the fabricated devices. The measured eye diagrams are clear and wide-open, and the bit error rate measurements show reasonable power penalties, indicating good device performance.

1. Introduction

Global Internet traffic is predicted to reach an annual data rate of 4.8 zettabytes per year by 2022.[1] Driven by the explosive growth of data traffic, modern data centers, and long-haul communication systems increasingly rely on optical interconnects to carry more data while consuming less energy.[2,3] Almost all optical interconnects consist of components fulfilling the same basic functions, particularly lasers, electro-optic modulators, optical (de)multiplexers, and photodetectors. Thanks to the mature fabrication processes developed by microelectronics industry, silicon photonics can accommodate the integration of these active and passive components on the same chip.[4,5] Commercial 400 Gbps silicon photonics optical transceivers have been developed,[6,7] which will drive the next-generation optical interconnects in data centers. However, the high-speed modulation in silicon photonics is typically achieved by the plasma dispersion effect

X. Han, Y. Jiang, H. Xiao, P. Zhang, J. Yang, Y. Tian
Institute of Microelectronics and Key Laboratory for Magnetism and Magnetic Materials of MOE
School of Physical Science and Technology
Lanzhou University
Lanzhou, Gansu 730000, China
E-mail: siphoton@lzu.edu.cn

A. Frigg, T. G. Nguyen, A. Boes, G. Ren, A. Mitchell
Integrated Photonics and Applications Centre (InPAC)
School of Engineering
RMIT University
Melbourne VIC 3001, Australia
E-mail: guanghui.ren@rmit.edu.au

A. Frigg
Department of Production
Ligentec SA
Ecublens 1024, Switzerland

Y. Su
The State Key Laboratory of Advanced Optical Communication Systems and Networks
Department of Electronic Engineering
Shanghai Jiao Tong University
Shanghai 200240, China

The ORCID identification number(s) for the author(s) of this article can be found under https://doi.org/10.1002/lpor.202100529

DOI: 10.1002/lpor.202100529

of silicon, which requires doping of the silicon-on-insulator (SOI) platform.[8,9] The absorption losses and temperature sensitivities induced by the p-n junctions, can be a limiting factor for the performance of SOI modulators.

Recently, lithium niobate on insulator (LNOI) has emerged as an attractive technology for photonic integrated circuits (PICs) with the development of the crystal ion slicing technology.[10] The LNOI platform can take full advantage of lithium niobate to implement high-speed electro-optic modulators and optical nonlinear devices, while offering high index-contrast waveguide and tight optical confinement for high-density integration simultaneously.[11–14] For example, electro-optic modulators on the LNOI platform have been demonstrated with modulation frequencies in excess of 100 GHz,[15,16] and with CMOS compatible driving voltages.[17] To achieve the full potential of LNOI as a PIC platform, there is still a need to develop passive components for monolithic integration with the active components. However, there remain some challenges associated with the direct etching of LNOI. For example, the etch depth of the lithium niobate thin film is limited with respect to the available lithography resists, and the Ar+ milling process requires significant optimization and maintenance to achieve low-loss waveguides. Further, the direct etching forms slanted waveguide sidewalls limiting the minimum spacing between neighboring waveguides, which is not conducive to realize devices based on strongly coupled waveguides (e.g. directional coupler).[14] Thus, the LNOI platform still lacks some passive PIC components, which have been demonstrated in other PIC platforms and are of equal importance.

Optical (de)multiplexer is one of the key passive PIC components as they enable parallel transmission of multiple data channels in an optical waveguide or fiber, which are essential to improve the data capacity of optical interconnects. In SOI platform, many (de)multiplexing technologies have been demonstrated, including wavelength-division multiplexing (WDM),[18] mode-division multiplexing (MDM),[19] and polarization-division multiplexing (PDM).[20] Among them, WDM is the most-developed technology, which is successfully used in commercial optical transceivers. However, WDM requires the integration of multiple laser sources, which can be complex and expensive. In recent years, the MDM and PDM technologies have attracted significant attention, as different-order modes and different light polarization offer new optical dimensions to carry data, requiring only a single-wavelength laser source. This has motivated a large number of experimental demonstrations of mode and polarization (de)multiplexers in SOI platform, which can dramatically enhance the data capacity of on-chip data communication systems.[21–26] It is particularly attractive to integrate the optical (de)multiplexing devices with high-speed optical modulators in a LNOI platform to achieve high-capacity and low-cost PICs suitable for data communication applications. However, so far there are only a few works reported for MDM and PDM devices in LNOI platform.

In this contribution, we investigate and demonstrate mode and polarization (de)multiplexers by introducing silicon nitride as a loading material to the surface of LNOI platform.[27–30] Compared to lithium niobate, silicon nitride has a slightly lower refractive index which is important to achieve a strong mode confinement in lithium niobate, similar transparency window, very low material loss, and commercially available fabrication processes. Thus, the silicon nitride loaded LNOI platform offers an attractive choice for combining active and passive components to achieve multi-functional, high-performance, and low-cost PICs for future high-speed optical interconnects, while avoiding the direct etching of lithium niobate. We considered the birefringence of lithium niobate and waveguides along Z and Y crystallographic directions in a silicon nitride loaded LNOI (X-cut) platform. As a proof-of-concept demonstration, we successfully design, fabricate and demonstrate a four-mode (de)multiplexer (MMUX) along the crystallographic Z direction and a polarization splitter-rotator (PSR) along the crystallographic Y direction based on the asymmetrical directional coupler (ADC) structure. The measured insertion losses are less than 1.46 dB and 1.49 dB, while the intermodal crosstalk is lower than −13.03 dB and −17.75 dB for the MMUX and PSR, respectively. Furthermore, we transmitted 40 Gbps modulated data on different mode and polarization channels to characterize the data processing capabilities of the devices. The measured bit error ratio (BER) results show reasonable power penalties, indicating the good performance of the devices. This work is expected to provide guidelines for future designs of MDM and PDM devices in the LNOI platform.

2. Modal Behaviors along Different Crystallographic Directions of Lithium Niobate

In this work, we choose a X-cut LNOI platform to have the crystallographic Z direction in the plane of lithium niobate thin-film to enable access to the strong electro-optic coefficient (r_{33}) and second-order nonlinear coefficient (d_{33}) for future applications. The X-cut LNOI wafer has a 300-nm-thick lithium niobate layer. To laterally confine the optical mode, we used a 300 nm of silicon nitride layer, in accordance with our previous work.[31] The mode confinement factor (Γ_{LN}) in lithium niobate is calculated to be ≈60% for a silicon nitride width of 1 μm by using the finite element method,[32] which is comparable to the values reported previously for electro-optic modulation.[29,30] As shown in **Figure 1**, the birefringence of lithium niobate means that light polarized along crystallographic Z direction experiences the extraordinary refractive index (n_e) of ≈2.138, while light polarized along the crystallographic X and Y directions experiences the ordinary refractive index (n_o) of ≈2.211, at the wavelength of 1550 nm. This leads to different effective refractive indices of optical modes when propagating along different waveguide directions. Thus, the waveguide directions need to be considered carefully when designing mode and polarization multiplexing devices in the LNOI platform. To understand the modal behavior better, we calculate the mode effective indices as a function of waveguide width along Y and Z crystallographic directions at the wavelength of 1550 nm, respectively. The results obtained by a full-vector eigenmode solver are shown in Figure 1.[33]

Figure 1a shows the modal behavior for waveguides along crystallographic Y direction (Y-propagating), where the following observations can be made: i) the effective index difference between different-order modes with the same polarization is only about one-tenth when compared to the SOI platform due to the lower index contrast of the waveguide in the LNOI platform;[21,22] ii) the effective indices of TM modes are close to that of TE modes, even though the TM modes have stronger evanescent field outside the waveguide than TE modes. This is caused by the TE

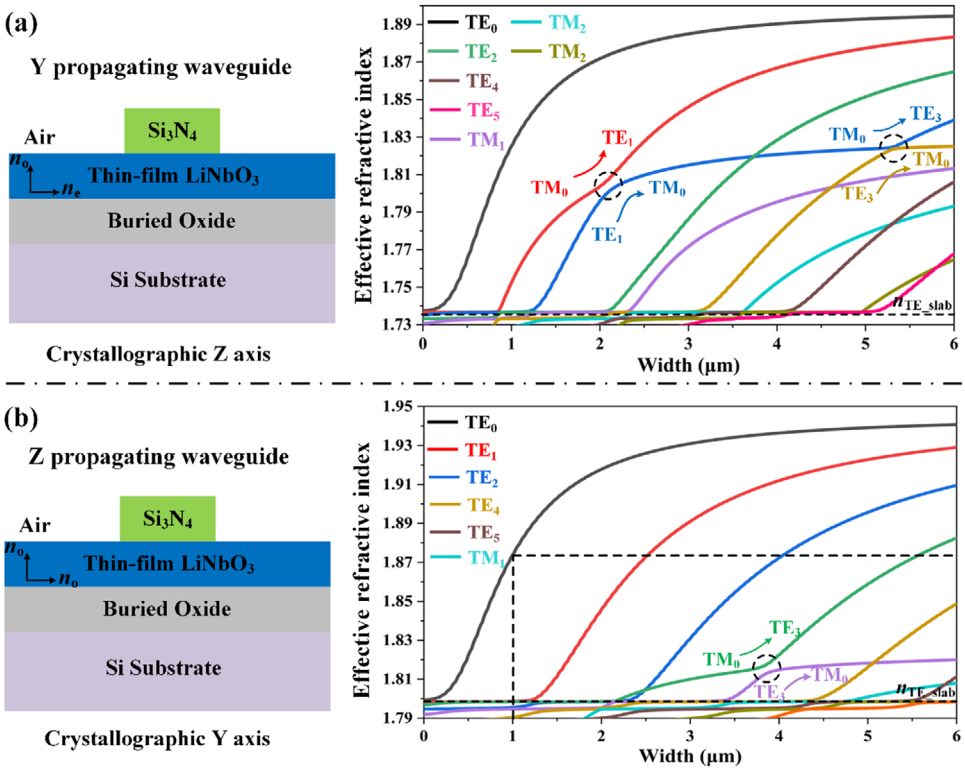

Figure 1. The cross-sectional views of a) Y propagating and b) Z propagating waveguides and the corresponding mode effective indices as a function of waveguide widths.

modes are mainly experiencing n_e, while TM modes experience the larger n_o; iii) mode hybridizations can occur at some waveguide widths, which are indicated by circles (refer to S1, Supporting Information for details), as the silicon nitride loaded LNOI rib waveguide is vertically asymmetrical.[24,25] The mode hybridization can be both an advantage and disadvantage. On the one hand, in a MMUX structure, the mode hybridizations can introduce high loss and inter-modal crosstalk due to coupling to undesired modes when the waveguide transitions between different waveguide widths. Even if one increases the single-mode waveguide width so that the phase-matching multimode waveguides can avoid the mode hybridization width, the effective index difference between different-order modes will be reduced (refer to S2, Supporting Information for details), leading to higher loss and inter-modal crosstalk.[34] Thus, Y-propagating waveguides are less attractive for the implementation of mode (de)multiplexers in the nitride loaded LNOI platform, especially for higher order modes. On the other hand, the mode hybridization can be used to realize polarization rotation which is essential to achieve a PSR structure as the mode hybridization can be used for efficient mode conversion between TM and TE modes when light propagates along the waveguide, with the appropriate width. One can also see that, the effective index of TM_0 mode is lower than the TE slab modes for waveguide widths below ≈0.85 μm, resulting in lateral leakage (refer to S3, Supporting Information for details). This causes the TM_0 mode to couple to radiating TE slab modes, leading to high propagating loss.[35]

Figure 1b shows the modal behavior for Z-propagating waveguides. One can see that the effective index difference between TE and TM modes is increased compared to the Y-propagating waveguide. This can be explained by the TE modes mainly experience n_o while TM modes have strong field components in both vertical and longitudinal directions and thus experience both n_o and n_e in the Z-propagating waveguides. This is attractive for the implementation of mode (de)multiplexers, as one can select a narrower single-mode waveguide width compared to Y-propagating waveguides to achieve phase matching with multimode waveguides and simultaneously avoid waveguide widths that cause mode hybridization. Thus, the effective index difference between different-order modes in the multimode waveguides remains large enough to realize low-loss and low-crosstalk mode coupling, even for very-high-order modes. This makes Z-propagating waveguides more suitable to implement MMUXs in the silicon nitride loaded LNOI platform.

3. Simulation and Design

3.1. Simulation and Design of the Mode (De)Multiplexer

As a proof of concept, we first propose and design a four-mode MMUX (TE_0 ≈ TE_3) based on cascade ADC structures along the crystallographic Z direction. A 3D schematic of the device is shown in **Figure 2**a. In the device, the first four TE modes are multiplexed to a multimode waveguide for parallel transmission, and then, demultiplexed to corresponding ports for measurements. Figure 2b shows a top view of the investigated ADC-based MMUX including the indicated structural parameters. The ADC-based mode converters are key components of the

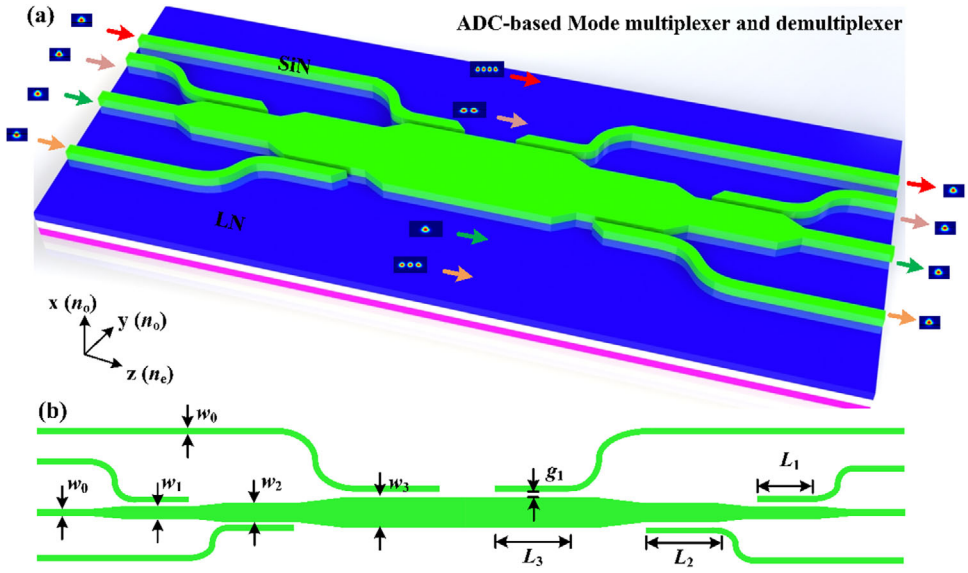

Figure 2. a) The 3D schematic of the investigated ADC-based MMUX. b) The top view of the investigated ADC-based MMUX with marked structural parameters.

investigated MMUX, which need to be designed carefully. In this work, the widths of the single-mode waveguides are chosen to be w_0=1 μm which can enable relatively low waveguide loss under the TE single-mode condition (refer to S4, Supporting Information for details). According to the phase-matching condition,[22] the corresponding widths of the multimode waveguides carrying TE_1, TE_2, and TE_3 modes are w_1=2.528 μm, w_2=4.059 μm and w_3=5.59 μm, respectively, which have been indicated by black dash lines in Figure 1b. A waveguide bending radius of 150 μm is used to separate the input of the single-mode waveguides from the multimode waveguides. All coupling gaps between the single-mode and multimode waveguides are set to g_1=0.2 μm. Using the finite-difference time domain (FDTD) method,[32] and taking the effects of the bending waveguide into consideration, we optimized the coupling lengths for TE_0-to-TE_1, TE_0-to-TE_2, and TE_0-to-TE_3 mode conversions to be L_1=8 μm, L_2=16 μm, and L_3=23 μm, respectively. The simulated normalized transmission spectra at the wavelength of 1525–1565 nm for the mode conversions are shown in **Figure 3**a–c, with the corresponding E-field profiles at a wavelength of 1550 nm shown in Figure 3d–f.

It can be seen from the results that the conversion efficiency reaches −0.36 dB (>−0.39 dB), −0.44 dB (>−0.46 dB) and −0.62 dB (>−0.64 dB) for a wavelength of 1550 nm (in the whole 40 nm wavelength range), while the inter-modal crosstalk from adjacent order modes is −22.05 dB (<−21.39 dB), −16.36 dB (<−16.17 dB) and −13.38 dB (<−13.17 dB) for TE_1, TE_2 and TE_3 modes at the wavelength of 1550 nm (in the whole 40 nm wavelength range), respectively. To reduce the inter-modal crosstalk, the 150-μm-long taper waveguides are used to connect the multimode waveguides with different widths for adiabatic mode transitions.

3.2. Simulation and Design of the Polarization (De)Multiplexer

Second, we design a PSR based on the mode hybridization in a Y-propagating waveguide. In the real-world applications, the PSR can also be regarded as a polarization (de)multiplexer. **Figure 4** shows a 3D schematic with a top view of the proposed device consisting of a polarization rotator, a two-mode MMUX, and a TE polarizer. The detailed principle of the device is as follows: first, a TE_0 mode and a TM_0 mode are input into the polarization rotator, where the TM_0 mode will be converted to TE_1 mode due to the mode hybridization while the TE_0 mode remains unchanged. Then, the TE_0 mode and TE_1 mode will be demultiplexed in the MMUX, as the TE_1 mode will be coupled to the adjacent waveguide to a TE_0 mode due to phase matching. Finally, the TE polarizer is used at the through port to filter out the unconverted TM_0 mode for reducing crosstalk. As a result, the input TE_0 mode is directed to the through port, while the TM_0 mode is converted to a TE_0 mode at the cross port.

First, we optimize the polarization rotation section of the PDM. Similar to above, the width of the single-mode waveguide at the front end of the device is chosen to be w_4=1 μm. For the polarization rotator, the multimode waveguide width is set to w_5=2.1 μm, which is at the anti-crossing in Figure 1a and where the effective index difference between the TM_0 mode and the TE_1 mode is minimum. The length of the multimode waveguide is then optimized to L_4=100 μm by using the FDTD method. The simulated normalized transmission spectra in the wavelength range of 1525–1565 nm for the TM_0 and TE_0 excitation modes are shown in **Figure 5**a,b, respectively. The corresponding E-field profiles at a wavelength of 1550 nm are shown in Figure 5c,d. It can be seen from the results that the TM_0-to-TE_1 conversion efficiency reaches up to −0.14 dB (>−0.31 dB) at the wavelength of 1550 nm (in the whole 40 nm wavelength range), while the transmission loss of the TE_0 mode is negligible.

Next, we optimize the conversion of the TE_1 mode to TE_0 mode in the cross port. For the ADC-based TE_0-TE_1 MMUX, the width of the narrower single-mode waveguide is set to w_6=1.2 μm, and thus, the width of the phase-matching multimode waveguide is w_7=2.839 μm which is far away from the hybridization width. The coupling gap between the single-mode waveguide and

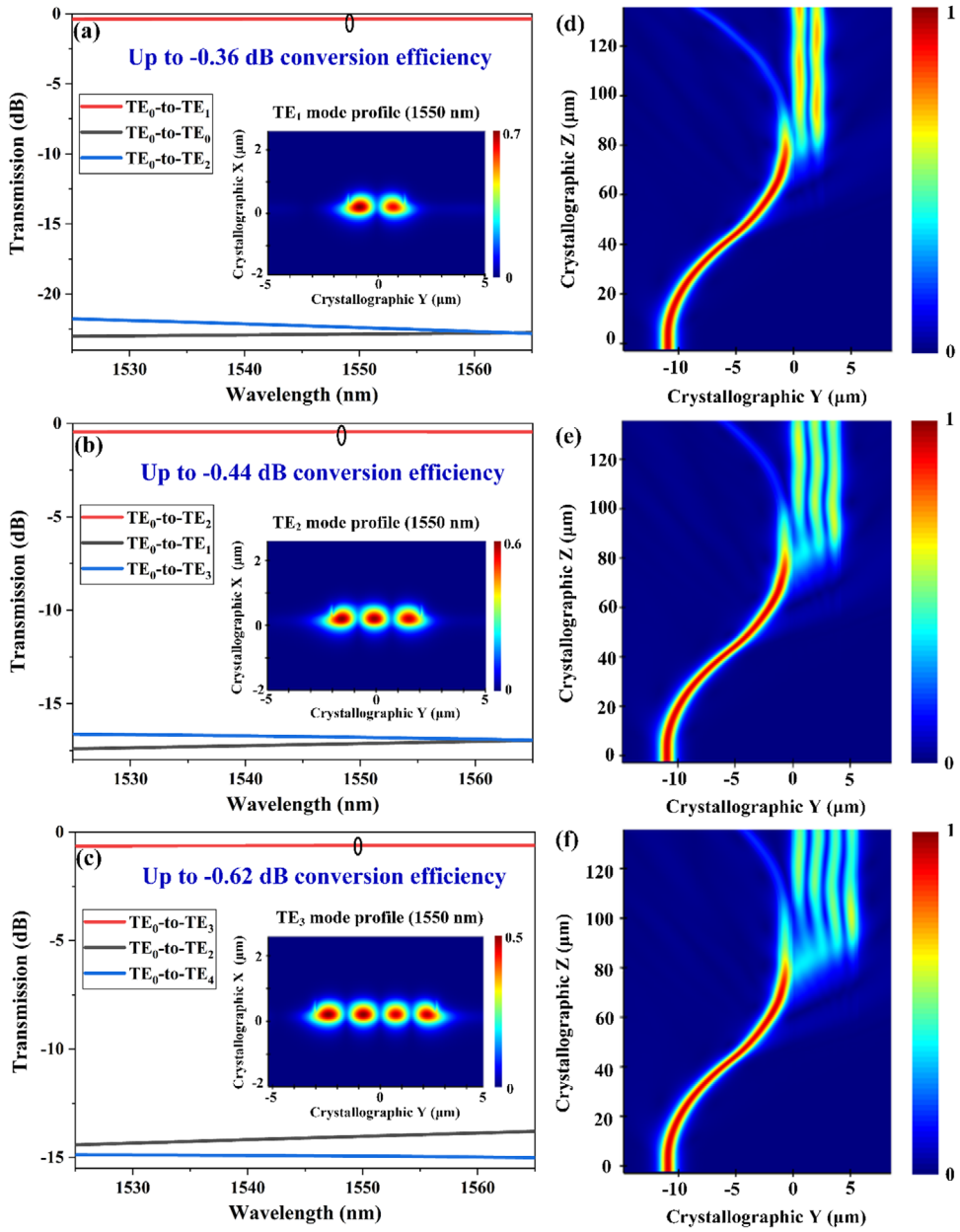

Figure 3. The simulated a–c) normalized transmission spectra with detected high order mode profiles and d–f) E-field profiles for TE_0-to-TE_1, TE_0-to-TE_2, and TE_0-to-TE_3 mode conversions, respectively, in the ADC-based mode converters.

multimode waveguide is set as g_2=0.2 μm, while the coupling length is optimized to be L_5=28 μm using the FDTD method again, considering the effect of the bend waveguide with a radius of 150 μm. The simulated normalized transmission spectra at the wavelength of 1525–1565 nm of the TE_1 and TE_0 modes input into the MMUX are shown in **Figure 6**a,b, with the corresponding E-field profiles at a wavelength of 1550 nm shown in Figure 6c,d. It can be seen that the excited TE_1 mode is converted to TE_0 mode at the cross port with a conversion efficiency of −0.10 dB (>−0.11 dB) at the wavelength of 1550 nm (in the whole 40 nm wavelength range), while the TE_0 mode mainly passes through the coupling region.

So far, a PSR is formed successfully by combining the polarization rotator and the TE_0-TE_1 MMUX along the crystallographic Y direction. However, there remains unconverted TM_0 mode in the waveguide (see Figure 5a), as the effective indices of TM_0 and TE_1 modes are not matched perfectly due to the wavelength dispersion, especially when the wavelength deviates from the central wavelength. The unconverted TM_0 mode can deteriorate the power extinction ratio between the through and cross ports, and hence decrease the working bandwidth of the device.[37] Thus, we propose to include a TE-pass polarizer to filter the TM_0 mode out. The TE polarizer is formed by a straight waveguide with a width of w_8=0.6 μm, where the transmission loss of the TM_0 mode at a

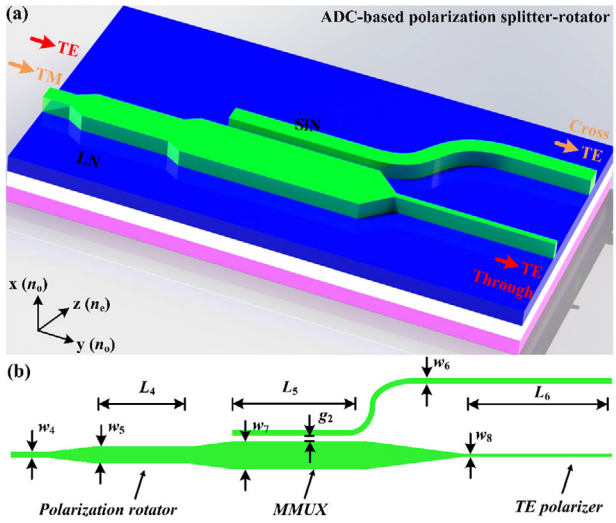

Figure 4. a) The 3D schematic of the investigated ADC-based PSR. b) The top view of the investigated ADC-based PSR with marked structural parameters.

wavelength of 1550 nm is estimated to be over 100 dB cm^{-1} due to the lateral leakage while the loss of TE_0 mode is negligible.[36] In this work, the length of the TE polarizer is set to L_6=300 μm, which can be further increased if higher extinction ratios are required. Linear tapered waveguides with optimized lengths are used to connect the straight waveguides with different widths. In Figure 4b, the lengths of the taper waveguides from left to right are set to 20, 20, and 150 μm, respectively.

4. Fabrication and Experimental Results

4.1. Fabrication and Characterization Setup

We fabricated the proposed devices on the same LNOI wafer provided by the "NANOLN." A close to stoichiometric silicon nitride thin film is deposited on the wafer by using the reactive sputtering.[37] Afterward, the devices are patterned by electron beam lithography (EBL) and inductively coupled plasma etching (ICP) processes. **Figure 7**a,b shows the micrograph of the fabricated MMUX and PSR, respectively. The devices are interfaced with grating couplers to couple light into and out of the chip (refer to S5, Supporting Information for details). The input and output ports of the MMUX are denoted as $I_0 \approx I_3$ and $O_0 \approx O_3$, respectively, corresponding to the coupling of the $TE_0 \approx TE_3$ modes into and out of the bus waveguide. Due to the polarization selectivity of the grating couplers, two PSRs with the same parameters are fabricated next to each other on the chip, while connecting to different grating couplers for TE and TM mode coupling. When launching the TE_0 mode in the PSR, the through and cross ports of the device are all connected to TE-type grating couplers as the polarization rotation is nearly negligible. When launching

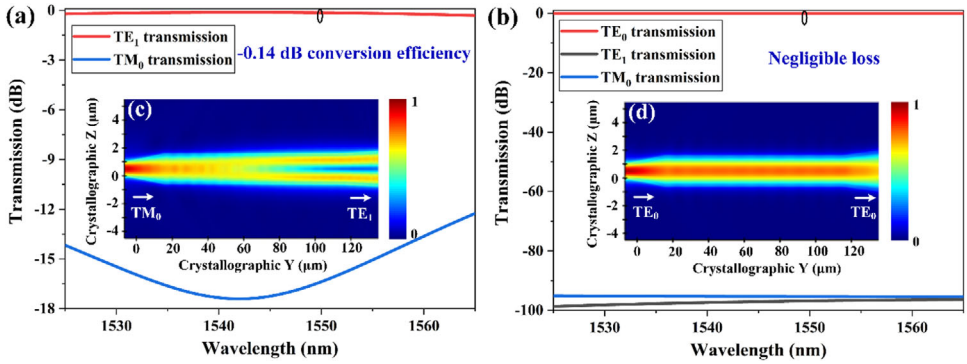

Figure 5. The simulated normalized transmission spectra at the wavelength of 1525–1565 nm for a) TM_0 and b) TE_0 modes input into the polarization rotator. The simulated E-field profiles at a wavelength of 1550 nm for c) TM_0 and d) TE_0 modes input into the polarization rotator.

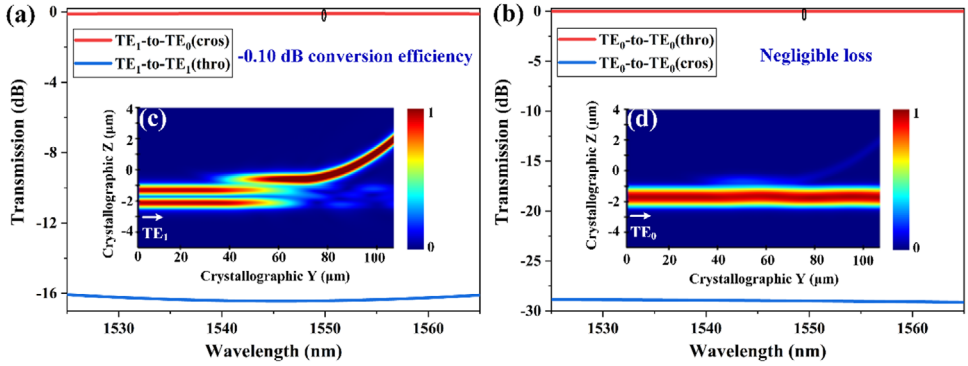

Figure 6. The simulated normalized transmission spectra at the wavelength of 1525–1565 nm for a) TE_1 and b) TE_0 modes input into the multimode waveguide of MMUX (cros, cross port; thro, through port). The simulated E-field profiles at a wavelength of 1550 nm for c) TE_1 and d) TE_0 modes multimode waveguide of MMUX.

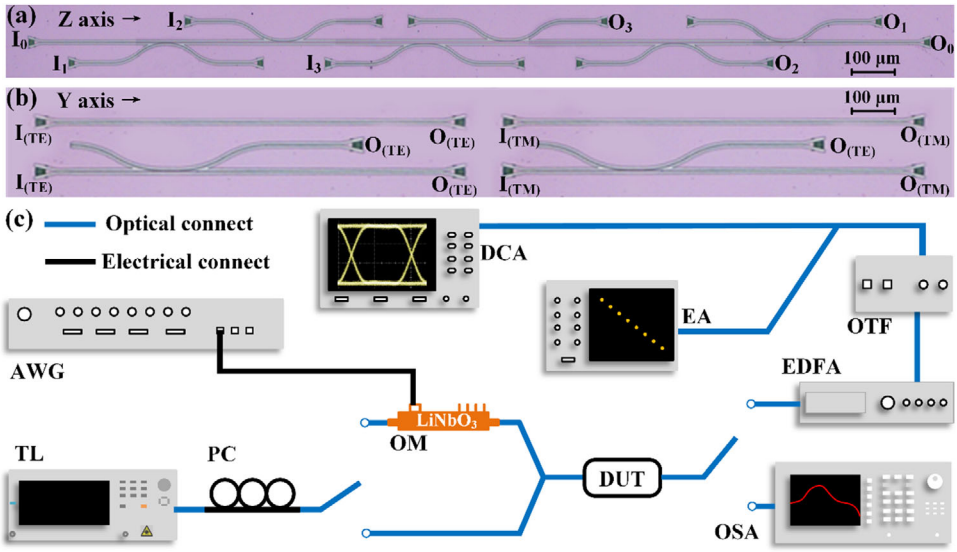

Figure 7. Optical microscope images of fabricated a) MMUXs and b) PSRs. c) Illustrations of the static and dynamic experimental setup. (TL, tunable laser; OM, optical modulator; PC, polarization controller; DUT, device under test; OSA, optical spectrum analyzer; EDFA, erbium-doped fiber amplifier; OTF, optical tunable filter; DCA, digital communication analyzer; AWG, arbitrary waveform generator; EA, error analyzer).

the TM_0 mode in the PSR, the through and cross ports of the device are connected to TM-type and TE-type grating couplers, respectively. Furthermore, reference straight waveguides are also fabricated next to the devices, which are interfacing to different grating couplers as well.

Static and dynamic measurements are carried out to characterize the performance of the fabricated devices. Schematics of the experimental setup are shown in Figure 7c. The static experimental setup is composed of a wavelength tunable laser (TL), a polarization controller (PC), and an optical spectrum analyzer (OSA). In the experiment, the laser light (1525–1565 nm) is first transmitted into the PC, and then coupled into and out of the chip via the input and output grating couplers, finally the transmission spectra are recorded by the OSA. The measured results are then normalized by using the transmission of the reference straight waveguide. The dynamic experimental setup is used to demonstrate the data transmission capabilities of the devices. As shown in Figure 7c, the laser light is first processed by the PC, and then modulated by a 40 Gbps pseudo-random binary sequence with a length of $2^{10}-1$ which is generated by the arbitrary waveform generator (AWG). After that, the modulated signal is coupled into and out of the chip with relatively low loss. The output signal is amplified by an erbium-doped fiber amplifier followed by an optical tunable filter to reduce the background noise. Finally, the optical signal is directed to a digital communication analyzer and an error analyzer with a photodetector for eye diagram and BER measurements, respectively. For clarity, only the results measured at 1550 nm are shown in the following sections.

4.2. Experimental Results for the MMUX

Figure 8 shows the results of the static characterization (measured transmission spectra) of the fabricated MMUX. The measured insertion losses are below 0.25 dB, 1.13 dB, 1.46 dB, and 0.71 dB, while the inter-modal crosstalk is below −18.01 dB, −13.03 dB, −14.84 dB, and −13.05 dB for the TE_0, TE_1, TE_2, and TE_3 mode channels, respectively. The insertion losses of TE_1 and TE_2 modes are larger than that of TE_3 mode, as the TE_1 and TE_2 modes could also be coupled slightly out of the bus waveguide through the TE_3 mode converters and this will incur some insertion loss for each component, while the TE_3 mode will not be affected by TE_1 and TE_2 mode converters.[21] The performance can be further improved by selecting a slightly narrower single-mode waveguide (e.g. 800 nm) as the effective index difference between different order modes in the multimode waveguides is enlarged (reducing the crosstalk).

The static characterization results in Figure 8 show lower than −10 dB inter-modal crosstalk which has been demonstrated to be small enough and has negligible influence on the dynamic measurement.[38] **Figure 9** shows the results of the dynamic characterization (measured eye diagrams and BERs) for different mode channels of the MMUX. It can be seen from Figure 9a that clear and open eyes are obtained for all mode channels, and the extinction ratio is larger than 11.37 dB. Figure 9b shows that the measured power penalties at a BER of 10^{-9} are 0.65, 0.09, 0.30, and 0.76 dB for TE_0, TE_1, TE_2, and TE_3 mode channels, respectively. The measured results indicate that such MMUX are suitable for future MDM communication applications in LNOI platform.

4.3. Experimental Results for the PSR

Figure 10 shows the results of the static characterization (measured transmission spectra) of the fabricated PSR. The measured insertion losses are lower than 0.85 dB and 1.49 dB, while the inter-modal crosstalk is lower than −17.75 dB and −26.02 dB for TE_0 and TM_0 modes input, respectively. It can be seen that the crosstalk for TM_0 mode input is much lower than that in the

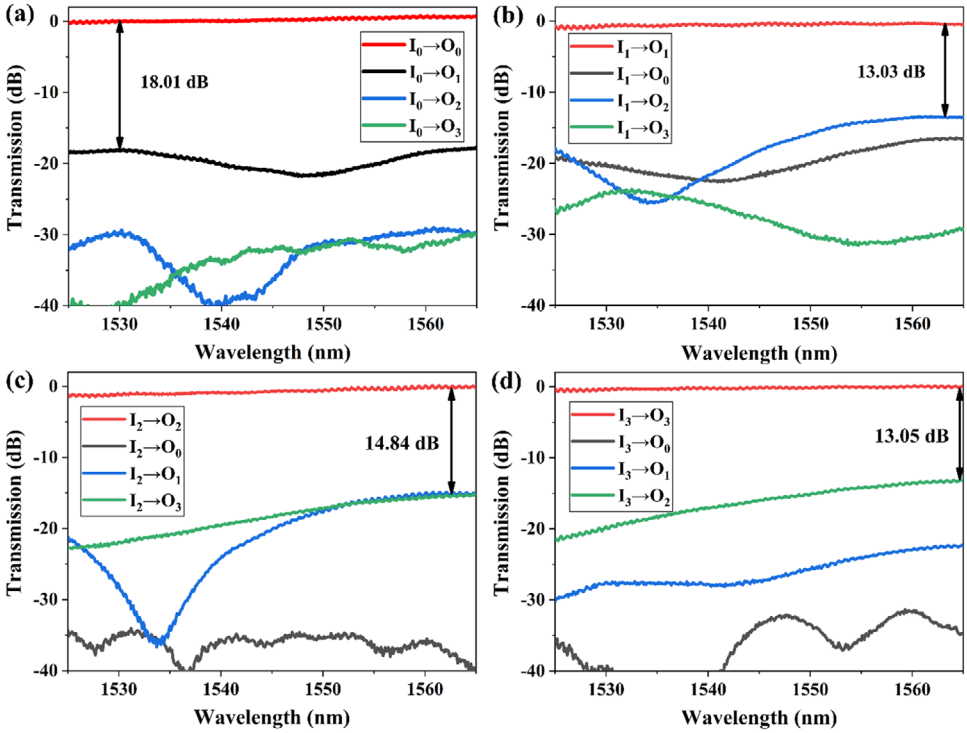

Figure 8. The measured transmission spectra at different output ports of the MMUX for light input at a) I_0, b) I_1, c) I_2 and d) I_3 ports, respectively.

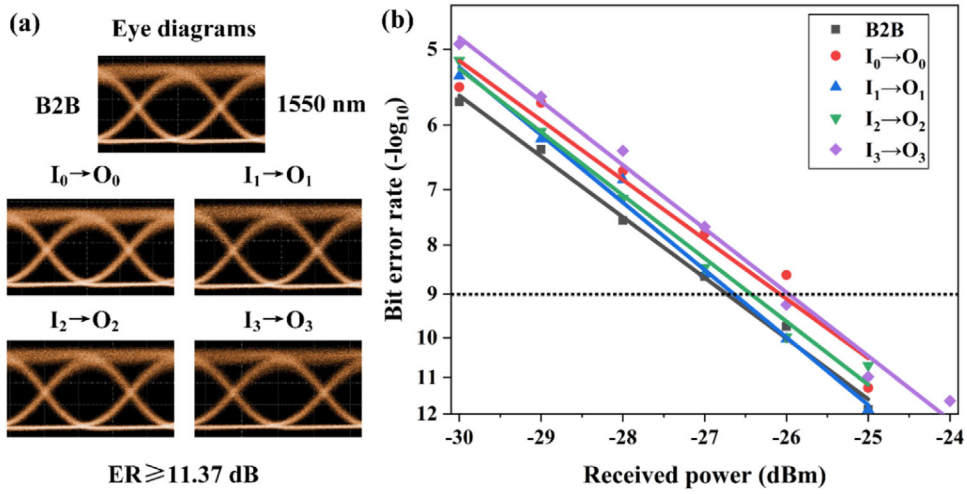

Figure 9. The measured a) eye diagrams and b) BERs in the 40 Gbps data transmission experiment for the fabricated MMUX.

simulation due to the use of TE-pass polarizer. The crosstalk for TE_0 mode input is then limited by the performance of the TE_0-TE_1 MMUX, and thus, higher than that for TM_0 mode input (refer to S6, Supporting Information for details).

Figure 11 shows the results of the dynamic characterization (eye diagrams and BERs) measured at the through and cross ports of the PSR for TE_0 and TM_0 modes input, respectively. The eyes are clear and open as well with the extinction ratio larger than 11.35 dB, as shown in Figure 11a. It can be seen from Figure 11b that the measured power penalties at a BER of 10^{-9} are 2.07 dB and 1.89 dB for TE_0 and TM_0 modes input, respectively. The experimental results indicate the good performance of the fabricated device.

5. Discussion

In this section, we provide a brief summary of the reported works focusing on MDM and PDM in the LNOI platforms.

For MDM, though Zhang et al. propose and demonstrate a reconfigurable two-mode (de)multiplexer on a direct etching LNOI platform recently,[39] the direct etching LNOI platform still lacks MDM demonstration with a moderate mode channel number

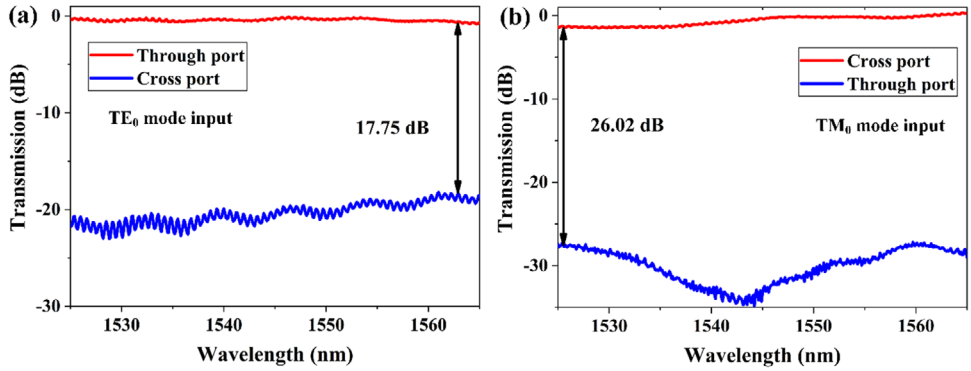

Figure 10. The measured transmission spectra at different output ports of the PSR for a) TE_0 and b) TM_0 modes input.

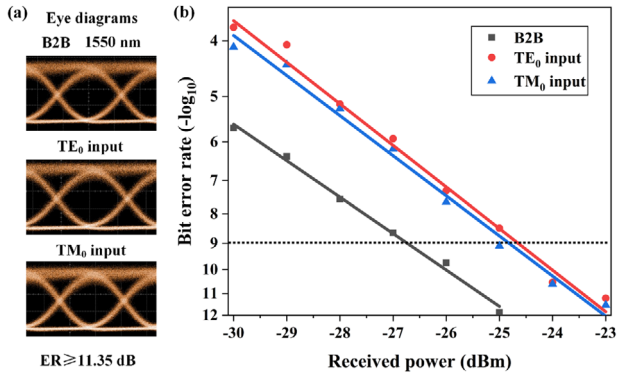

Figure 11. The measured a) eye diagrams and b) BERs in the 40 Gbps data transmission experiment for the fabricated PSR.

(≥4). As aforementioned, this case can be partially explained by that the direct etching forms slanted waveguide sidewalls limiting the minimum spacing between neighboring waveguides, which is not conducive to realize devices based on strongly coupled waveguides. This has also motivated researchers to realize MDM through other dielectrically loaded LNOI platforms. In 2020, Yu et al. experimentally demonstrated a four-channel TM mode (de)multiplexer by using bound states in the continuum (BICs) on a polymer loaded LNOI platform.[38] Though the demonstration is impressive, the BIC waveguide only guides light in specific polarization and wavelengths. The insertion loss is also not good because they could not achieve BIC state for all modes. Most recently, Liu et al. demonstrated a four-mode (de)multiplexer with TE modes based on a silicon rich nitride (SRN) loaded LNOI platform.[40] The device shows good performance. However, there are also several shortcomings to the demonstrated device: i) compared to lithium niobate, the SRN has a higher refractive index which will cause the mode to be mainly confined in the SRN loading, limiting the efficiency for electro-optic modulation or second harmonic generation due to the lower optical field overlap with the lithium niobate thin film; ii) compared to silicon nitride, the SRN material has a narrower material band gap, limiting the shortest wavelength that the waveguides can be used for.

We provide a brief summary of previously reported MMUX on the LNOI platform in **Table 1**. It can be seen that this work shows overall improvement in fabrication processes, supported light polarization and wavelength, mode confinement factor in lithium niobate layer, mode channel number, device insertion losses, and crosstalk.

On the other hand, to the best of our knowledge, this work is the first demonstration for PDM in the LNOI platform.

Table 1. Performance of reported mode (de)multiplexers in the LNOI platform.

Ref.	Etching of LN	BIC	Γ_{LN}	Mode number	Maximum insertion loss (1550 nm)	Maximum crosstalk (1550 nm)
[39]	Yes	No	High	2	/	/
[38]	No	Yes	High	4	2.80 dB	−13.80 dB
[40]	No	No	Low	4	1.60 dB	−18.46 dB
This work	**No**	**No**	**High**	**4**	**0.63 dB**	**−14.70 dB**

6. Conclusion

In this work we investigated MDM and PDM technologies in a X-cut silicon nitride loaded LNOI platform. According to the analysis of mode properties in this platform, the MDM and PDM are developed along crystallographic Z and Y directions, respectively. For a proof of concept, the ADC-based MMUX and PSR are designed, fabricated, and experimentally demonstrated. The measured transmission spectra show large bandwidth, low insertion loss, and low crosstalk for the fabricated devices. To demonstrate the data transmission capabilities of the devices, we obtained clear and open eye diagrams and the BER measurements show reasonable power penalties when transmitting 40 Gbps. To the best of our knowledge, this work is the first demonstration of MDM and PDM in the silicon nitride loaded LNOI platform. Besides, this work is expected to pave the way for high-speed and large-capacity optical interconnects based on the LNOI platform.

Supporting Information

Supporting Information is available from the Wiley Online Library or from the author.

Acknowledgements

This work was supported by National Natural Science Foundation of China (NSFC) (62075091), China Postdoctoral Science Foundation (2020M673533), Open Project Program of Wuhan National Laboratory for Optoelectronics (2019WNLOKF003), and Australian Research Council (ARC) grants (DP190102773, DP190101576). The authors acknowledge the facilities, and the scientific and technical assistance, of the Micro Nano Research Facility (MNRF) and the Australian Microscopy & Microanalysis Research Facility at RMIT University. This work was performed in part at the Melbourne Centre for Nanofabrication (MCN) in the Victorian Node of the Australian National Fabrication Facility (ANFF).

Conflict of Interest

The authors declare no conflict of interest.

Data Availability Statement

The data that support the findings of this study are available from the corresponding author upon reasonable request.

Keywords

lithium niobate on insulator, mode-division multiplexing, polarization-division multiplexing, silicon nitride

Received: September 16, 2021
Published online:

[1] C. Forecast, in *Cisco visual networking index: Forecast and trends, 2017–2022*, Cisco public information, **2019**.
[2] S. Rumley, M. Bahadori, R. Polster, S. D. Hammond, D. M. Calhoun, K. Wen, A. Rodrigues, K. Bergman, *Parallel Comput.* **2017**, *64*, 65.
[3] P. J. Winzer, D. T. Neilson, A. R. Chraplyvy, *Opt. Express* **2018**, *26*, 24190.
[4] W. Bogaerts, L. Chrostowski, *Laser Photonics Rev.* **2018**, *12*, 1700237.
[5] R. Won, *Nat. Photonics* **2010**, *4*, 498.
[6] E. Timurdogan, Z. Su, R.-J. Shiue, M. J. Byrd, C. V. Poulton, K. Jabon, C. DeRose, B. R. Moss, E. S. Hosseini, I. Duzevik, M. Whitson, R. P. Millman, D. A. Atlas, M. R. Watts, in *Optical Fiber Communication Conference*, Optical Society of America, New York **2020**, p. T3H. 2.
[7] H. Yu, P. Doussiere, D. Patel, W. Lin, K. Al-Hemyari, J. Park, C. Jan, R. Herrick, I. Hoshino, L. Busselle, M. Bresnehan, A. Bowles, G. A. Ghiurcan, H. Frish, S. Yerkes, R. Venables, P. Seddighian, X. Serey, K. Nguyen, A. Banerjee, S. A. Asl, Q. Zhu, S. Gupta, A. Fuerst, A. Dahal, J. Chen, Y. Malinge, H. Mahalingam, M. Kwon, S. Gupta, in *Optical Fiber Communication Conference*, Optical Society of America, New York **2020**, p. T3H. 6.
[8] E. Timurdogan, C. M. Sorace-Agaskar, J. Sun, E. S. Hosseini, A. Biberman, M. R. Watts, *Nat. Commun.* **2014**, *5*, 4008.
[9] M. Li, L. Wang, X. Li, X. Xiao, S. Yu, *Photonics Res.* **2018**, *6*, 109.
[10] M. Levy, R. Osgood Jr, R. Liu, L. Cross, G. Cargill, III, A. Kumar, H. Bakhru, *Appl. Phys. Lett.* **1998**, *73*, 2293.
[11] G. Poberaj, H. Hu, W. Sohler, P. Guenter, *Laser Photonics Rev.* **2012**, *6*, 488.
[12] A. Boes, B. Corcoran, L. Chang, J. Bowers, A. Mitchell, *Laser Photonics Rev.* **2018**, *12*, 1700256.
[13] Y. Qi, Y. Li, *Nanophotonics* **2020**, *9*, 13.
[14] D. Zhu, L. Shao, M. Yu, R. Cheng, B. Desiatov, C. Xin, Y. Hu, J. Holzgrafe, S. Ghosh, A. Shams-Ansari, E. Puma, N. Sinclair, C. Reimer, M. Zhang, M. Lončar, *Adv. Opt. Photonics* **2021**, *13*, 242.
[15] M. Xu, M. He, H. Zhang, J. Jian, Y. Pan, X. Liu, L. Chen, X. Meng, H. Chen, Z. Li, X. Xiao, S. Yu, S. Yu, X. Cai, *Nat. Commun.* **2020**, *11*, 3911.
[16] P. Kharel, C. Reimer, K. Luke, L. He, M. Zhang, *Optica* **2021**, *8*, 357.
[17] C. Wang, M. Zhang, X. Chen, M. Bertrand, A. Shams-Ansari, S. Chandrasekhar, P. Winzer, M. Lončar, *Nature* **2018**, *562*, 101.
[18] R. Nagarajan, C. H. Joyner, R. P. Schneider, J. S. Bostak, T. Butrie, A. G. Dentai, V. G. Dominic, P. W. Evans, M. Kato, M. Kauffman, *IEEE J. Sel. Top. Quantum Electron.* **2005**, *11*, 50.
[19] C. Li, D. Liu, D. Dai, *Nanophotonics* **2018**, *8*, 227.
[20] T. Barwicz, M. R. Watts, M. A. Popović, P. T. Rakich, L. Socci, F. X. Kärtner, E. P. Ippen, H. I. Smith, *Nat. Photonics* **2007**, *1*, 57.
[21] D. Dai, J. Wang, Y. Shi, *Opt. Lett.* **2013**, *38*, 1422.
[22] L.-W. Luo, N. Ophir, C. P. Chen, L. H. Gabrielli, C. B. Poitras, K. Bergmen, M. Lipson, *Nat. Commun.* **2014**, *5*, 3069.
[23] H. Xiao, Z. Liu, X. Han, J. Yang, G. Ren, A. Mitchell, Y. Tian, *Opt. Express* **2018**, *26*, 22366.
[24] D. Dai, J. E. Bowers, *Opt. Express* **2011**, *19*, 10940.
[25] H. Xu, Y. Shi, *Opt. Express* **2017**, *25*, 18485.
[26] Y. Zhang, Y. He, X. Jiang, B. Liu, C. Qiu, Y. Su, R. A. Soref, *APL Photonics* **2016**, *1*, 091304.
[27] S. Jin, L. Xu, H. Zhang, Y. Li, *IEEE Photonics Technol. Lett.* **2015**, *28*, 736.
[28] A. Rao, A. Patil, P. Rabiei, A. Honardoost, R. DeSalvo, A. Paolella, S. Fathpour, *Opt. Lett.* **2016**, *41*, 5700.
[29] A. N. R. Ahmed, S. Nelan, S. Shi, P. Yao, A. Mercante, D. W. Prather, *Opt. Lett.* **2020**, *45*, 1112.
[30] A. N. R. Ahmed, S. Shi, A. Mercante, S. Nelan, P. Yao, D. W. Prather, *APL Photonics* **2020**, *5*, 091302.
[31] A. Boes, L. Chang, M. Knoerzer, T. G. Nguyen, J. D. Peters, J. E. Bowers, A. Mitchell, *Opt. Express* **2019**, *27*, 23919.
[32] A. W. Snyder, J. D. Love, in *Optical Waveguide Theory*, Springer, New York **1983**, pp. 601–622.
[33] T. G. Nguyen, R. S. Tummidi, T. L. Koch, A. Mitchell, *IEEE Photonics Technol. Lett.* **2009**, *21*, 486.
[34] H. A. Haus, *Waves and Fields in Optoelectronics*, Prentice-Hall, Hoboken, NJ **1984**.
[35] T. G. Nguyen, A. Boes, A. Mitchell, *IEEE J. Sel. Top. Quantum Electron.* **2019**, *26*, 1.
[36] Y. Liu, X. Huang, Z. Li, Y. Kuang, H. Guan, Q. Wei, Z. Fan, Z. Li, *Opt. Lett.* **2020**, *45*, 4915.
[37] A. Frigg, A. Boes, G. Ren, I. Abdo, D.-Y. Choi, S. Gees, A. Mitchell, *Opt. Express* **2019**, *27*, 37795.
[38] Z. Yu, Y. Tong, H. K. Tsang, X. Sun, *Nat. Commun.* **2020**, *11*, 2602.
[39] M. Zhang, K. Chen, M. Wang, J. Wu, K. S. Chiang, *Opt. Lett.* **2021**, *46*, 1001.
[40] Y. Liu, X. Huang, Z. Li, H. Guan, Z. Yu, Q. Wei, Z. Fan, W. Han, Z. Li, *Opt. Lett.* **2021**, *46*, 3179.